Transport properties of supercooled confined water

F. Mallamace[1,2,a], C. Branca[1], M. Broccio[1], C. Corsaro[1], N. Gonzalez-Segredo[1], J. Spooren[1], H.E. Stanley[3], and S.-H. Chen[2]

[1] Dipartimento di Fisica and CNISM, Università di Messina, 98166 Messina, Italy
[2] Department of Nuclear Science and Engineering, Massachusetts Institute of Technology, Cambridge, MA 02139, USA
[3] Department of Physics, Center for Polymer Studies, Boston University, Boston, MA 02215, USA

Abstract. This article presents an overview of recent experiments performed on transport properties of water in the deeply supercooled region, a temperature region of fundamental importance in the science of water. We report data of nuclear magnetic resonance, quasi-elastic neutron scattering, Fourier-transform infrared spectroscopy, and Raman spectroscopy, studying water confined in nanometer-scale environments. When contained within small pores, water does not crystallise, and can be supercooled well below its homogeneous nucleation temperature T_h. On this basis it is possible to carry out a careful analysis of the well known thermodynamical anomalies of water. Studying the temperature and pressure dependencies of water dynamics, we show that the liquid-liquid phase transition (LLPT) hypothesis represents a reliable model for describing liquid water. In this model, water in the liquid state is a mixture of two different local structures, characterised by different densities, namely the low density liquid (LDL) and the high-density liquid (HDL). The LLPT line should terminate at a special transition point: a low-T liquid-liquid critical point. We discuss the following experimental findings on liquid water: (i) a crossover from non-Arrhenius behaviour at high T to Arrhenius behaviour at low T in transport parameters; (ii) a breakdown of the Stokes-Einstein relation; (iii) the existence of a Widom line, which is the locus of points corresponding to maximum correlation length in the p-T phase diagram and which ends in the liquid-liquid critical point; (iv) the direct observation of the LDL phase; (v) a minimum in the density at approximately 70 K below the temperature of the density maximum. In our opinion these results represent the experimental proofs of the validity of the LLPT hypothesis.

1 Introduction

Water is certainly the most essential of any molecules on Earth. Understanding the role of water in many aspects of life represents one of the most challenging research problems in science and technology. Despite many centuries of research the properties of water are far from being completely understood. The large number of anomalies, more than sixty, that distinguish water from other liquids lack a coherent explanation, so water is considered an "unicum" in nature. The liquid state of water is unusual especially at low temperatures in the supercooled regime [1–3]. In this state, thermodynamic response functions such as compressibility, thermal expansion coefficient, and specific heat, display counterintuitive trends as the temperature is lowered. In particular, while the anomalies displayed by liquid water are apparent above the melting temperature, T_m, they become more striking as one supercools below T_m. Ordinarily,
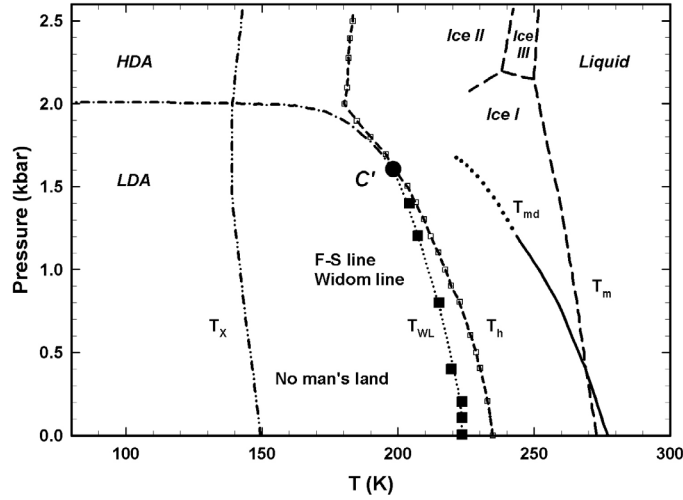
[a] e-mail: `francesco.mallamace@unime.it`

Fig. 1. The phase diagram of water in the $p-T$ plane (redrawn from [2,3]). T_h denotes the homogeneous nucleation temperature line, T_x the crystallisation line of amorphous water, T_m the melting temperature line and T_{md} the maximum density line. T_{WL} indicates the Widom line locus.

it has been suggested that water behaves as if there exists a singular temperature toward which its thermodynamical properties diverge [1]. In fact, extrapolated from their values at moderately supercooled states, all these functions appear to diverge at a singular temperature around $T_S = 228$K. Over the years, many plausible explanations for these strange behaviours have been proposed, starting from the two-state and the clathrate models [1–3]. Three hypotheses are currently of active interest: (i) the stability limit [4], (ii) the percolation [5] and (iii) the liquid-liquid phase transition (LLPT) [6]. The third approach has received support from various theoretical studies [7–9]. However, in all of them the key role is played by the local hydrogen bond (HB) interaction pattern having a tetrahedral geometry. In the liquid state this HB network governs the overall structure and dynamics [3] of water.

Water has also an intriguing pressure-temperature $(p-T)$ phase diagram (Fig. 1), characterised by specific regions of existence of the liquid, solid and amorphous phases. In the Fig. 1, T_m is the melting temperature line, and T_h represents the homogeneous nucleation temperature line for bulk water, whereas T_{md} corresponds to the temperature line of maximum density. Water can exist in a glassy form at the lowest temperatures. Depending on T and p, glassy water has two amorphous phases with different structures: a low (LDA) and a high (HDA) density amorphous ice; thus it shows a polyamorphism. LDA can be formed from HDA and vice versa; LDA if heated, undergoes a glass-to-liquid transition transforming into a highly viscous fluid, then crystallises into cubic ice at T_X. Thus an experimentally inaccessible T region exists in bulk water between T_h and T_X. Such a region between glassy and liquid phase of water, in which bulk water does not exist as a liquid, was named "No Man's Land" [3]. The existence of two glassy phases, which correspond to two different local tetrahedral arrangements, is a characteristic property of water; in typical liquids we do not find two different glassy phases. The transition from the LDA to the HDA is a first-order phase transition [10,11]. As well explained in H.E. Stanley's contribution in the present issue, on the basis of the LLPT hypothesis there is the reasonable idea that the separation line of the two amorphous forms of solid water extends into the No Man's Land and ultimately terminates at a critical point. Just as the glassy water first-order transition line separates LDA from HDA, its extension into the liquid region separates a low-density liquid (LDL) from a high-density liquid (HDL) phase. The existence of a LLPT leads to conjecture that liquid water possesses a low-T liquid-liquid critical point, C', (predicted by the theory to be located at $T_c \approx 200$ K $p_c \approx 1$ kbar) [2], below which it can switch from one phase, HDL, to another phase, LDL. The difference between the two liquid phases lies in the water structure: in the HDL, the local tetrahedrally coordinated hydrogen-bond network is not fully developed, whereas in the LDL a more open, locally ice-like

hydrogen-bond network is fully developed [12]. Thus, near T_c, water is a mixture of both LDL and HDL phases associated with a diverging density fluctuation. At higher temperatures, the two liquid phases are indistinguishable. Lowering temperature or increasing pressure will result in an increase of the LDL phase with respect to the HDL phase. The LLPT approach suggests to focus careful interest on the so called Widom line, i.e. the locus of the maximum correlation length [13]. The existence of a critical point induces large fluctuations in a region that extends to temperatures and pressures far away in the phase diagram. For example, experiments show that the effect of the gas-liquid critical point C on the thermodynamic response functions is evident even at a temperature twice as high than the critical one. A similar behaviour is expected also for the hypothesised critical point C'. Above T_c the response functions have an extreme (minimum or maximum) at the Widom line. On decreasing T, the Widom line converges to the critical point, where the correlation length diverges together with the response functions. Therefore, along the Widom line, the response functions show extremes and finally diverge at the critical point. Since far above a critical point the maxima of correlation length and the extremes of response functions become smooth and flat, the Widom line is broadened in a region whose size increases at higher T. As a consequence, different response functions show extremes along different lines, all around the Widom line and all converging at the critical point.

Up to few years ago, the phase diagram reported in Fig. 1, together with the fashioning physic scenario proposed by the LLPT hypothesis (and in particular the Widom line), especially for the experimental difficulties to explore the No Man's Land, remained only hypothesised, but not completely proved. The power-law approach, considered for many years to explain water singularities, corresponds to the extension of a first-order transition line beyond the critical point. Thus the thermodynamical response functions, when experimentally approaching the Widom line, should behave, as though they are going to diverge with critical exponents but does not. However, computer simulations, using tried and tested models for liquid water, confirm the broad features of this phase diagram [14]. Recently, a possibility to enter into the inaccessible temperature range of water, is shown by confining water in nano-size pores [15–17]. When contained within these pores, water does not crystallise, and can be supercooled well below $T_h = 231$ K. Porous hydrophilic silica glass [17], micellar systems or layered vermiculite clay [15] are examples of confining nano-structures. Using this trick we were able to study, by means of different experimental techniques like, Neutron scattering, Nuclear Magnetic Resonance (NMR) and Raman and/or Fourier Transform Infrared (FTIR) spectroscopy, the structural and dynamical properties of water in the temperature range 170 K $< T < 290$ K. In such a way, in recent experiments [18,19] on confined water as a function of temperature and pressure we showed that the theoretical LLPT approach is able to describe coherently some of the strange properties of water. By using the neutron scattering technique, an evidence of the LL critical point, C', located at $T_C = 200$ K and $p_C = 1.6$ kbar was obtained.

Subsequently this result was also qualitatively confirmed by an extensive MD simulation analysis [20]. In particular, in this MD study by using three different models (namely: TIP5P, ST2 and the Jagla potential) the loci of maxima of the relevant water response functions (compressibility and specific heat), which coincide close to the critical point and give rise to the Widom line, have been evaluated. These experiments [18–20] are of primary interest because, for their findings, have stimulated much of the recent work on water. It has been suggested that a significant change in water dynamics takes place in deeply supercooled state [21–23]. Unlike other network forming materials, water behaves, in the experimentally accessible window, as a non-Arrhenius fluid (fragile glass former). Based on analogies with network forming liquids and with the properties of the amorphous forms of water, it has been proposed that, at ambient pressure, liquid water should show a dynamical crossover from non-Arrhenius at high T to Arrhenius (strong glass former) behaviour at low T [24]. The study of Refs. [18–20] focused on this fragile-to-strong dynamic crossover (FSC) pointing out, in a general way, the connections among the Widom line and the FSC and associating the crossing of the Widom line with the changes in the HB structure of liquid water. It has been evidenced that upon crossing the Widom line on decreasing T, a breakdown of the Stokes-Einstein relation (BSE) is observed at $T < T_{WL}(P)$ (where T_{WL} is the Widom line temperature) [25]. Both the phenomena, FSC and BSE, take place at T_{WL} and are related with the changes in water structural and dynamical

properties from those of HDL to LDL. The LDL phase has been observed for the first time in a recent FTIR experiment [26]. It is thus possible that other new phenomena can appear to occur in water on crossing this line, all of them being related to the changes in the local water structure that occur when the system changes from the "HDL-like" side to the "LDL-like" side. Beside the FSC and the BSE, both accompanied by evident changes in the dynamic transport properties, such as the diffusion coefficient and the relaxation time, it is possible that water presents other phenomena on crossing the Widom line. Examples are: (i) systematic changes in the static structure factor $S(q)$, and the corresponding pair correlation function $g(r)$, revealing that, according to the FTIR results [26], for $T < T_{WL}$, the system structure resembles more that of LDL than HDL, (ii) the appearance, for $T < T_{WL}$, of a shoulder (Boson peak) in the dynamic structure factor $S(q, \omega)$ at a frequency $\omega \approx 60\,\mathrm{cm}^{-1}$ [27,28], (iii) a rapid increase in hydrogen bonding degree for $T < T_{WL}$ [29,30], (iv) a minimum in the density at low temperature [31,32], and (v) a scaled equation of state near the critical point C' [33]. In this work, we report recent experimental findings on water related with the hypothesised LLPT, and with the effects on the water properties induced by the presence of the LDL local structure. In particular we give a review of the FSC, the BSE, the observation, by means of local vibrational modes of the $S(q, \omega)$, of the LDL phase and finally the observation, by means of scattering methods, of a water density minimum in the very supercooled region at about $200\,\mathrm{K}$. We highlight that these results are entirely connected to the changes of the water local structure when the system evolves from the HDL to the LDL phase.

2 Experimental methods

2.1 The sample

To confine water we used a micelle template mesoporous silica matrix MCM-41-S (having 1D cylindrical tubes arranged in a hexagonal structure), synthesised using the methods of zeolite seeds [18]. The investigated samples have hydration levels of $h \simeq 0.5$ (0.5 grams H_2O per gram of MCM). As shown by X-ray diffraction (XRD) [34], differential scanning calorimetry (DSC) [35] and NMR [36,37] experiments, this water confining system can be regarded as one of the most suitable adsorbent models currently available. The geometrical constraints and the chemistry of the guest material surface may significantly affect the structure and dynamics of confined water. Examples are pore channel intersections (with networking effects), pore polydispersity, charges and chemical impurities. These phenomena reveal their presence with a marked hysteresis in a cooling/warming cycle. In MCM-41 nano-tube samples here studied, as shown by X-ray [34], and DSC experiments [35], the hysteresis is absent or negligible. DSC shows that repeated freezing and melting cycles (FMC) did not cause any significant change in the position and shape of DSC peaks for a given sample; the melting temperature was reproducible even after several months. Thus, water, in repeated FMC, does not affect the pore walls of these silica samples. In addition, the XRD data through the diffracted wave-vector, Q_0, of the first sharp water diffraction peak, give the following results: water in MCM-41 with a pore diameter $\phi = 42\text{\AA}$ have a sudden freezing at $T \approx 232\,\mathrm{K}$, whereas for $\phi = 24\text{\AA}$, it remains in a liquid state down to $\sim 160\,\mathrm{K}$. Moreover, in the MCM-41-S samples water freezes with a Q_0 value that is nearly the same as that of the LDA phase ($Q_0^{ice\text{-}c} = 1,71\,\text{\AA}^{-1}$) [38], in contrast to the stable ice-h, usually obtained by freezing bulk water ($Q_0^{ice\text{-}h} = 1,6\,\text{\AA}^{-1}$) [1]. In both the samples no Bragg's peaks, characteristic of crystallisation, are observed.

2.2 Nuclear magnetic resonance

Dynamical properties of water confined in fully hydrated MCM-41-S samples with $\phi = 24, 18$ and $14\,\text{\AA}$, were studied at ambient pressure and different temperatures by using a Bruker AVANCE NMR spectrometer, operating at $700\,\mathrm{MHz}$ ^{1}H resonance frequency. In these NMR experiments, we have measured the self-diffusion coefficient of water D, and the maximum intensity I^{max} of the ^{1}H-NMR spectra (obtained by the free-induction decay (FID)). The explored temperature range was 190K–298 K with an accuracy of ± 0.2K. D was measured with the pulsed gradient spin-echo technique (^{1}H-PGSE).
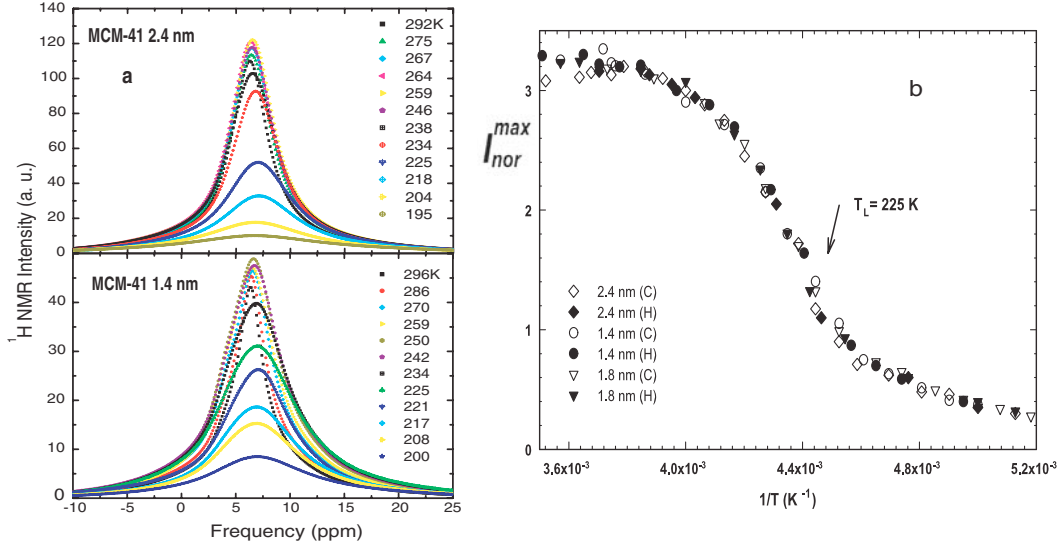
Fig. 2. (Colour online) (a) the ^{1}H NMR spectra of water in MCM samples with $\phi = 24$ and $14\,\text{Å}$, upon cooling. (b) The normalised NMR intensities, $I_{Nor}^{\max}$ vs. $1/T$, for $\phi = 14, 18$, and $24\,\text{Å}$ samples, upon both cooling and heating, corrected for the Curie effect (taken from [19]).

The ^{1}H NMR spectra of water in MCM samples with $\phi = 24$ and 14 Å, upon cooling are shown in Fig. 2(a). The full width at half-height of these spectra, $\Delta\nu_{1/2} \sim 1/T_2^*$, is the rate of the so-called *apparent* spin-spin relaxation time T_2^*. As it can be observed, the maximum intensity of the spectra ($I^{\max}$) decreases and the corresponding linewidth increases upon decreasing T; the crystalline ice phase (characterised by a very large linewidth) is not observed. The NMR signal intensity is directly related with the system equilibrium magnetisation, M_0 (or the susceptivity χ_0) which depends linearly on the total number of mobile spins per unit volume, the mean square value of nuclear magnetic moment and on $1/T$ (Curie law). Fig. 2(b) shows $I^{\max}$, for $\phi = 14, 18$ and 24 Å samples, upon both cooling and heating, corrected for the Curie effect and normalised to the pore volume, as $I_{Nor}^{\max}$ vs. $1/T$. As it can be noticed, the T behaviour of confined water is independent of the pore size. The figure clearly shows that there is a steep decrease of $I_{Nor}^{\max}$ on decreasing T, at around 225 K (T_L). This behaviour indicates that $T \sim 225$ K is a crossover temperature for the dynamical behaviour of water. In general, relaxations measured in an NMR experiment are caused by random fluctuations of the magnetic field at the position of a resonating spin originating by the thermal motion of neighboring spins. In our case the fluctuating magnetic dipole-dipole interactions between ^{1}H spins are due to the tumbling of molecules under the local caging structure. Hence, the observed behaviour of $I_{Nor}^{\max}$ can be related, according to the LLPT hypothesis, to the water structure and in particular to its packing density. The probability of tumbling of a water molecule is higher in the HDL phase, compared to that in the LDL phase; the temperature behaviour of $I_{Nor}^{\max}$ shown in Fig. 2(b) reflects just such a situation, indicating $T \sim 225$ K as the possible crossover temperature between the HDL and the LDL.

2.3 Neutron scattering

The water dynamics has been investigated in the $p - T$ phase diagram with incoherent quasi-elastic neutron scattering (QENS). Because of the exponential slowing down of water dynamics upon supercooling, the combined application of a time-of-flight (TOF) and a backscattering spectrometer has been necessary to study water from $T = 235$ K down to $T = 200$ K. The collected data have been analysed according to the relaxing cage model (RCM) [40]. QENS measurements were performed at NIST centre for Neutron Research using a disk chopper (DCS)
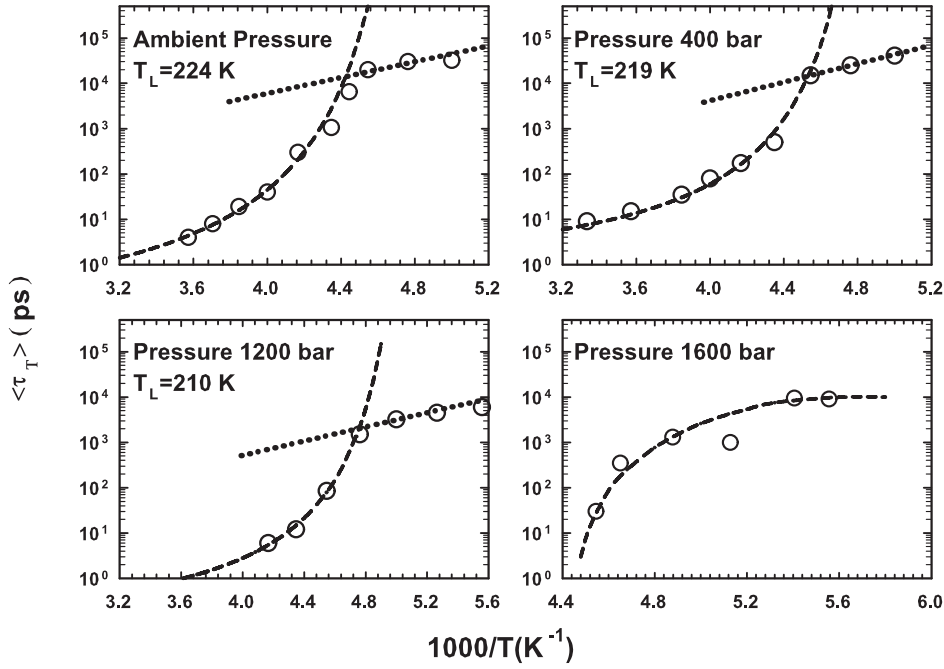
Fig. 3. Typical QENS results of hydrated MCM samples ($\phi = 14\,\text{Å}$) fitted in terms of the RCM analysis (Ref. [18]). The temperature dependence of $\langle\tau_T\rangle$, at different pressures, plotted in a log-lin scale vs $1/T$. A well-defined FSC is observed for $p < 1600$ bar.

and a backscattering (HFBS) spectrometer. The QENS experiments give the double differential scattering cross section $d^2\sigma/d\Omega d\omega$, where $E = \hbar\omega$ is the energy transferred by the neutron to the sample and $d\Omega$ is the scattering solid angle. $d^2\sigma/d\Omega d\omega$ is proportional to the dynamic structure factor $S(Q,\omega)$, which is the Fourier transform of the self-intermediate scattering function (ISF) and Q is the scattered wavevector. In such a way the ISF of the hydrogen atoms $F_H(Q,t)$, that in the investigated $Q-t$ range is $F_H(Q,t) \approx F_T(Q,t)\cdot F_R(Q,t)$, can be measured. F_T and F_R are the translational and the rotational ISF, respectively [40]. According to RCM, the translational and rotational dynamics of supercooled water can be separated in a short-time and in a long-time part. Thus F_T can be written as $F_T(Q,t) \approx F_T^s(Q,t)\exp[-(t/\tau_T)^\beta]$, whereas the $Q-t$ dependence of F_R can be written in terms of the well-known Sears expansion[41] as: $F_R(Q,t) = \sum_{l=0}^{\infty}(2l+1)j_l^2(Qb)C_l(t)$, with $j_l^2(Qb)$ being the Bessel function negligible for $Q \leq 2\,\text{Å}^{-1}$. Thus $C_1(t) = C_1^*(t)\exp[-(t/\tau_R)^\beta]$. Since translational and rotational dynamics are strongly coupled, the long-time behaviour of F_T and C_l coincide at specific Q_l values, independent of T. The RCM approach has been used to fit the neutron spectra according to the equation: $S(Q,\omega) = pR(Q_0,\omega) + (1-p)F.T.\{F_H(Q,t)R(Q_0,t)\}$, The parameter p represents the area of the elastic contribution arising from the MCM material. Because it has been found [40] that τ_T obeys to the power law $\tau_T = \tau_0(aQ)^{-\gamma}$, the measured spectra, recorded at any T, have been fitted, using four parameters τ_0, τ_R, γ, and β, with satisfactory results. From τ_0 and β the average relaxation time $\langle\tau_0\rangle = (\tau_0/\beta)\Gamma(1/\beta)$ shown in Fig. 3 has been obtained.

2.4 Fourier transform infrared spectroscopy

FTIR absorption measurements were performed at ambient pressure in the HOH bending and O-H stretching (OHS) vibrational spectral regions, by using a Bomem DA8 Fourier transform spectrometer. The investigated samples were the same as those of QENS and NMR experiments. The obtained spectra, are reported in Figs. 4(a) and (b). It must be noticed that the HOH bending spectra have a Gaussian-like form quite different from the nearly flattened form typical of polycrystalline ice, revealing that confined water remains in its liquid state in all the studied

T-range (Fig. 4(a)). Scattering methods have been largely used to study structural and dynamical properties of water and constitute the most used experimental approach to understand its properties. Indeed, neutron [12,18], X-ray [42], Raman and IR [43–46] scattering, have given evidence that water is characterised by the presence of two coexisting main HB structural phases, involving hydrogen bonded (HB) and non hydrogen bonded (NHB) molecules, respectively. Thus, it became customary to analyse OHS spectra by considering two general classes of O-H oscillators. These classes encompass broad Gaussian components, each referring to structures that involve a range of bond angles and distances distributed around the component peak position [46]. The spectral deconvolution was made by using a best fit procedure. In the fitting process all the spectral parameters were left to be free. We notice that the corresponding Full Widths Half Maximum (FWHM) and intensities (integrated areas) show changes whereas the wave-numbers fluctuate within the experimental error ($\pm 20 \, cm^{-1}$). Figure 4(c) reports also the fitting results.

OHS spectra of water, as measured by Raman scattering and Infrared absorption in the range $30 \, K < T < 647 \, K$ (i.e. from the LDA phase to nearly the first critical point of water), have been described by the following Gaussian component peak positions (wave-numbers) [46]: (I) $3120 \, cm^{-1}$, (II) $3220 \, cm^{-1}$, (III) $3400 \, cm^{-1}$, (IV) $3540 \, cm^{-1}$ and (V) $3620 \, cm^{-1}$ (within an experimental error of $\pm 20 \, cm^{-1}$). All of them have been unambiguously classified as HB or NHB OHS oscillators. The situation may be summarised as follows (see e.g. Fig. 4(c)):

(i) component I dominates the intensity of the LDA phase [47] so that it represents the OHS contribution of water molecules forming the "random tetrahedral network" (RTN);

(ii) components II and III have been associated with water molecules having an average degree of connectivity larger than that of monomers, but lower than that involved in the HB networks. Thus, they can be identified as partially HB (PHB) molecules [43,44,46];

(iii) components IV and V, being the only ones present in the Raman and IR spectra of bulk water in the T region near the first critical point ($630 \, K < T < 647 \, K$), arise from NHB monomeric water (or to molecules poorly connected to their environment) [43,46]. The integrated intensities of PHB and NHB water show an opposite temperature behaviour for $T > 300K$. While the intensities of NHB increase with increasing T, the ones of PHB decrease.

The classification of these contributions reflects the one used in the percolation hypothesis for water (f_i species of water, with i indicating the number of bonds) [5]. Thus, the HB component I is f_4, the NHB components IV and V are f_0, and finally PHB components II and III are f_1, f_2 and f_3. We have to stress that according to the LLPT hypothesis, the HDL phase is represented by both the NHB and PHB.

3 The FSC and BSE

Figure 3 reports, in a log-linear plot, the temperature variation of the average translational relaxation time $\langle \tau_T \rangle$ for water molecules, obtained by the QENS spectra using the relaxing cage model (RCM), at different pressures. Figure 3 deals with the thermal behaviour of $\langle \tau_T \rangle$ for pressures in the range $1 < p < 1600 \, bar$. It can be seen a transition from a Vogel-Fulcher-Tamman (VFT) law, $\langle \tau_T \rangle = \tau_0 \exp(BT_0/(T - T_0))$, where B is a constant providing the measure of fragility and T_0 the ideal glass transition temperature, to an Arrhenius law, $\langle \tau_T \rangle = \tau_0 \exp(E_A/k_B T)$, where E_A is the activation energy for the relaxation process. This transition from a VFT to an Arrhenius behaviour is the signature of the FSC dynamic transition. The crossover temperature T_L is calculated by $1/T_L = 1/T_0 - Bk_B/E_A$. Summarising all the results, in Fig. 1 the observed pressure dependence of T_L (squares) and its estimated continuation, denoted by a dashed line are reported. One should note that the T_L line has a negative slope, parallel to the T_{md} line, indicating a lower density liquid on the lower T side. This T_L line also approximately tracks the T_H line, and terminates in the upper end when intersecting the T_H line at 1660 bar and 200 K, at which point the character of dynamical transition changes. According to the previous results, confined water remains in the disordered liquid state both
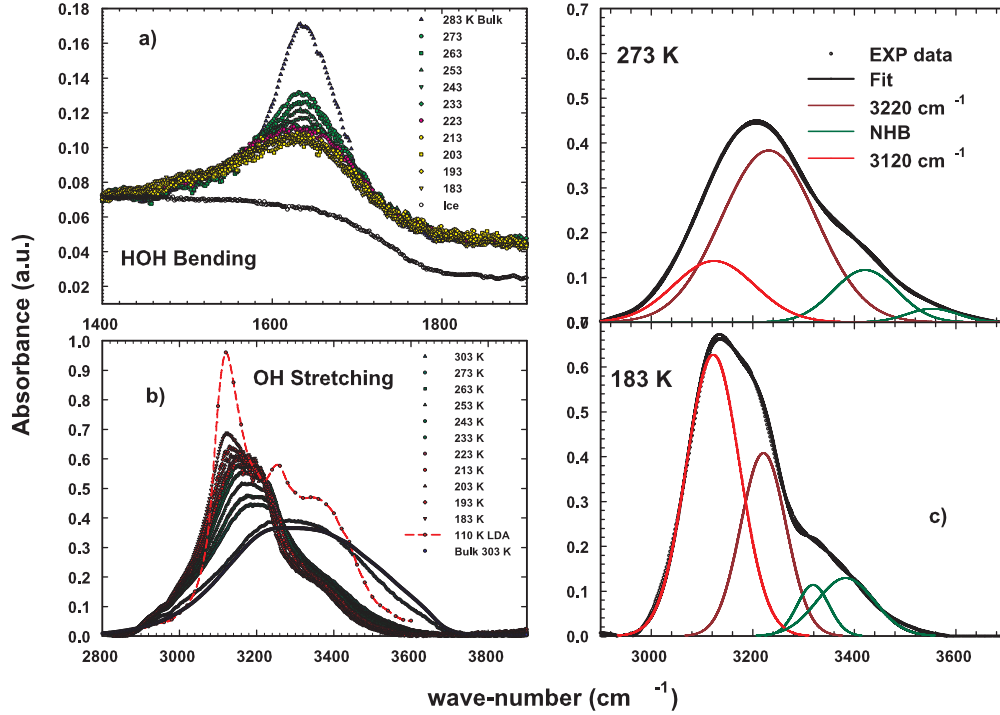
Fig. 4. (Colour online) (a) the HOH bending and (b) the O-H stretching (OHS) vibrational spectra of MCM confined water at the different investigated temperatures (taken from [26]). (c) Examples of the spectral fitting results.

above and below the FSC. Furthermore, by considering that the obtained activation energy barrier for initiating the local structure relaxation is $E_A = 5.4$ kcal/mol for the low-T strong liquid, it is reasonable to conclude that the high-T liquid corresponds to the HDL, while the low-T liquid to LDL. Thus, according to the MD simulation study [20], the FSC transition observed at T_L is caused by the crossing of the Widom line and that $T_L \equiv T_{WL}$. Well different is the $\langle \tau_T \rangle$ behaviour for $p > 1600$ bar, Fig. 3. At these high pressures the cusp-like behaviour characterising the FSC is not observed. In terms of the LLPT, and of its critical point, C', above the critical temperature T_C and below the critical pressure p_C, we are in the one-phase region, whereas for $p > p_C$ there is the two-phase region. Thus an experiment made in this "mixed state", on crossing the LL coexistence line, is not characterised by the large fluctuations observed in the one phase region. In this latter case the thermal behaviour of $\langle \tau_T \rangle$ does not show a clear-cut FSC. Such a picture explains the dynamical behaviour reported in Fig. 3, in which a clear FSC is observed up to 1400 bar and beyond 1600 bar the crossover is rounded off. These results indicate that the liquid-liquid critical point, C', can be located at $T_C = (200 \pm 10)$ K and $p_C = (1600 \pm 300)$ bar (Fig. 1).

Figure 5 shows the $\langle \tau_T \rangle$ (QENS data) as a function of $1/T$ (Fig. 5(a)) and the inverse of the self-diffusion coefficient of water $1/D$ measured at ambient pressure by NMR (Fig. 5(b)) for the fully hydrated MCM-41-S samples with pore diameters of 14 Å and 18 Å. As it can be observed, the measured values of D and $\langle \tau_T \rangle$ are independent of the pore size of the samples. This indicates that NMR field-gradient measurements, having a length scale larger than the sizes of the pores, are insensitive to the system geometry. In both the figures, the solid line denotes the data fit to the VFT law whereas the short dotted line denotes the fit to the Arrhenius law. From the NMR data we have obtained: $1/D_0 = 2.4 \cdot 10^7$ (s/m^2), $B = 1.775$, and $T_0 = 187$ K, $E_A = 3.98$ kcal/mol and $T_L = 224.5$ K; whereas from the $\langle \tau_T \rangle$ data at the ambient pressure the corresponding measured values are: $T_0 = 200$ K, $E_A = 5.4$ kcal/mol, and $T_L = 225.8$ K. The agreement between NMR and QENS results is thus satisfactory, especially regarding the two relevant quantities E_A and T_L. We have to stress that the interpretation of the FSC transition
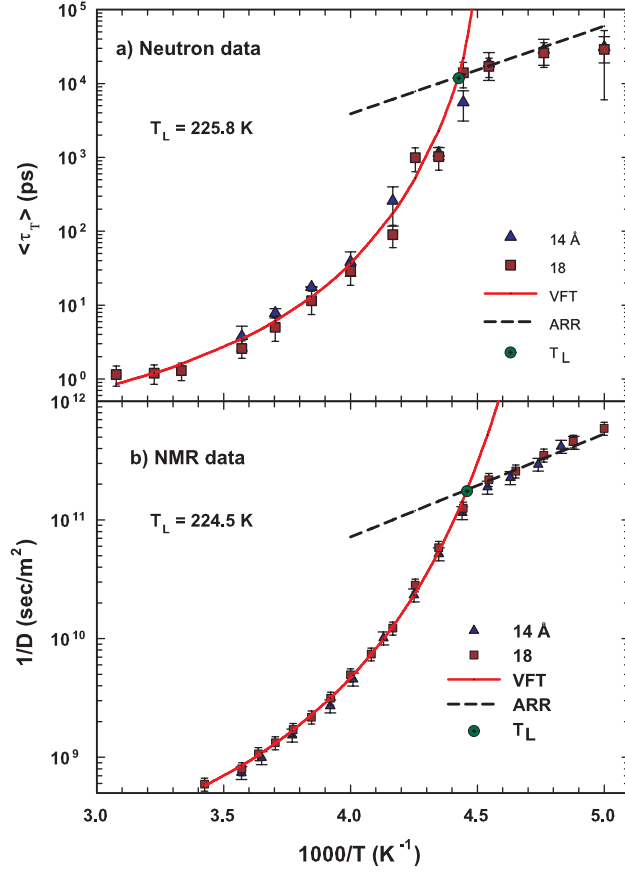
Fig. 5. (Colour online) (a) the $\langle \tau_T \rangle$ (QENS data) as a function of $1/T$. (b) The inverse of the self-diffusion coefficient $1/D$ of water measured at ambient pressure by NMR for the fully hydrated MCM-41-S samples with pore diameters of 14 Å and 18 Å. Solid lines mark fits of the VFT law to the experimental data, and the dotted lines are fits to the Arrhenius law (taken from [25]).

as a variant of the structural arrest transition (as predicted by the ideal mode coupling theory) was the essence of the QENS study of the structural relaxation time and MD study of the self-diffusion coefficient [18, 20]. The NMR results presented above thus constitute, by means of a direct measurement of the self-diffusion coefficient of supercooled water, an independent confirmation of the existence of FSC in water.

Let us now focus on the Stokes-Einstein relation (SE) that relates the self-diffusion coefficient D, viscosity η, and temperature T as $D \propto T/\eta$, which, as it is well known, is usually accurate for normal and high temperature liquids. Since $\langle \tau_T \rangle$ is proportional to the viscosity, we examine the relationship between D and $\langle \tau_T \rangle$ in the inset of Fig. 6, where the quantity $D\langle \tau_T \rangle/T$ is reported as a function of T. Triangles and squares represent its values coming from the experimental data of samples with $\phi = 14$ and $\phi = 18$ Å, respectively, whereas the dotted line represents the same quantity obtained using the corresponding fitting values reported in Figs. 5(a) and (b). The temperature dependence of $D\langle \tau_T \rangle/T$ shows that this quantity is constant at higher T, but increases steeply as T goes below the FSC temperature. Therefore, in the supercooled region the temperature behaviour of D and $\langle \tau_T \rangle$ is inconsistent with SE, signalling a marked decoupling between these two transport parameters, on decreasing T. In recent studies on some supercooled liquids, it has been reported that SE breaks down as the glass transition is approached. The water self-diffusion coefficient shows an enhancement of orders of magnitude from that expected from SE [48–52]. These decouplings of the transport coefficients, observed as a SE violation, have been attributed to the occurrence of dynamical heterogeneities in structural glass formers [48, 50, 53, 54]. Thus, in supercooled liquids there exist regions of varying dynamics,
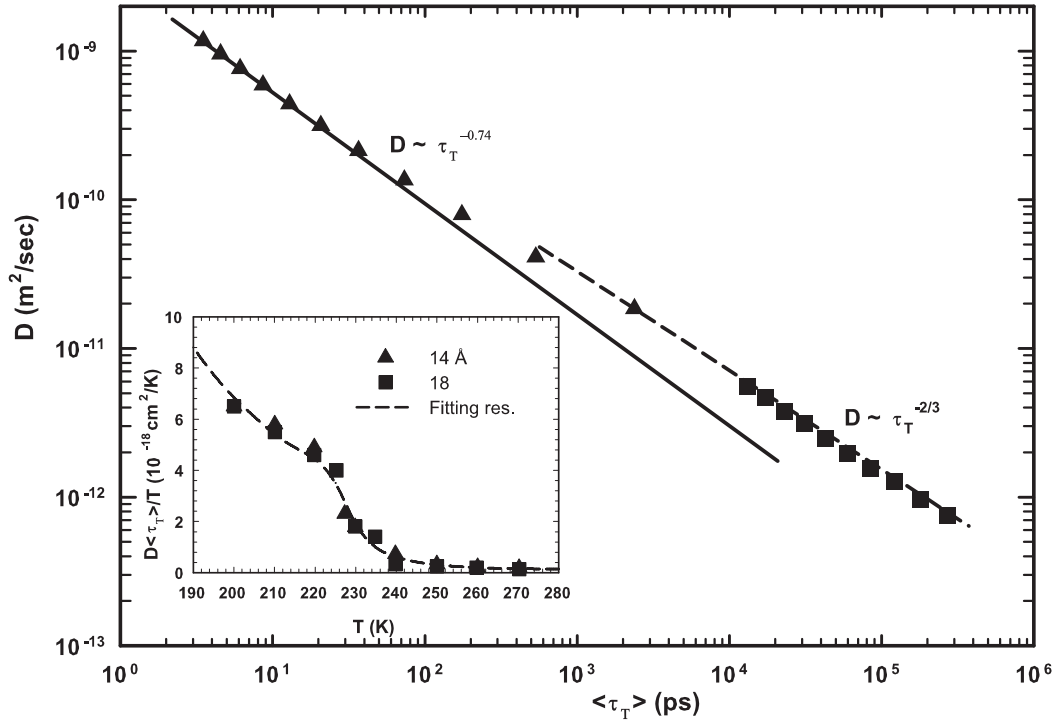
Fig. 6. Scaling representation of the BSE in a log-log scale of D vs. $\langle \tau_T \rangle$ (taken from [25]). Inset: $D\langle \tau_T \rangle / T$ vs. T, demonstrating the breakdown of the Stokes-Einstein relation.

i.e. fluctuations that dominate their transport properties near the glass transition. Furthermore, the non-monotonic variation of $D\langle \tau_T \rangle / T$ around the crossover region agrees with the theoretical findings reported by a recent study of the FSC using a kinetic lattice gas model [55].

The observed breakdown of the Stokes-Einstein relation (BSE) can be described using scaling concepts, in particular, the law $D \sim \tau^{-\xi}$, where $\xi = \alpha(T)/\beta(T)$ with α and β being temperature dependent scaling exponents of D and τ, respectively [56]. Recently, it has been shown that for tris-naphthylbenzene (a fragile glass former) $\xi = 0.77$ [50], whereas an MD simulation of Lennard-Jones binary mixture has given $\xi = 0.75$ [57]. By using such an approach, we will discuss our SE results for confined supercooled water. Figure 6 shows the D vs. $\langle \tau_T \rangle$ plot in a log-log scale, triangles represent data corresponding to temperatures above T_L, where water behaves as a fragile glass former, and squares pertain to the strong Arrhenius region. As it can be observed, the data clearly show two different scaling behaviours above and below the FSC temperature, in particular $\xi \simeq 0.74$ on the fragile side (dotted line) and $\sim 2/3$ on the strong side (solid line). These results agree with those of a recent theoretical study in which the decoupling of transport coefficients in supercooled liquids was investigated by using two classes of models, one describing diffusion in a strong glass former, and the other in a fragile one [56]. The main result of this study is that, while in the fragile case the SE violation is weakly dependent on the dimensionality d, with $\xi = 0.73$, in the strong case the violation is sensitive to d, going as $D \sim \tau^{-2/3}$ for $d = 1$, and as $D \sim \tau^{-0.95}$ for $d = 3$. On considering the geometry of the used confining system (1d cylindrical tubes, with a length of some μm and pore diameters of $\phi = 14\,\text{Å}$, and $18\,\text{Å}$), the scalings showed in Fig. 6 compare remarkably well with the findings of theoretical investigation [56], on both the fragile and strong sides.

4 The LDL phase and the water density minimum

The proof that the OHS spectral component (I) $3120\,\text{cm}^{-1}$ represents the LDL liquid phase is given on considering the temperature behaviour of its full width at half maximum (FWHM)
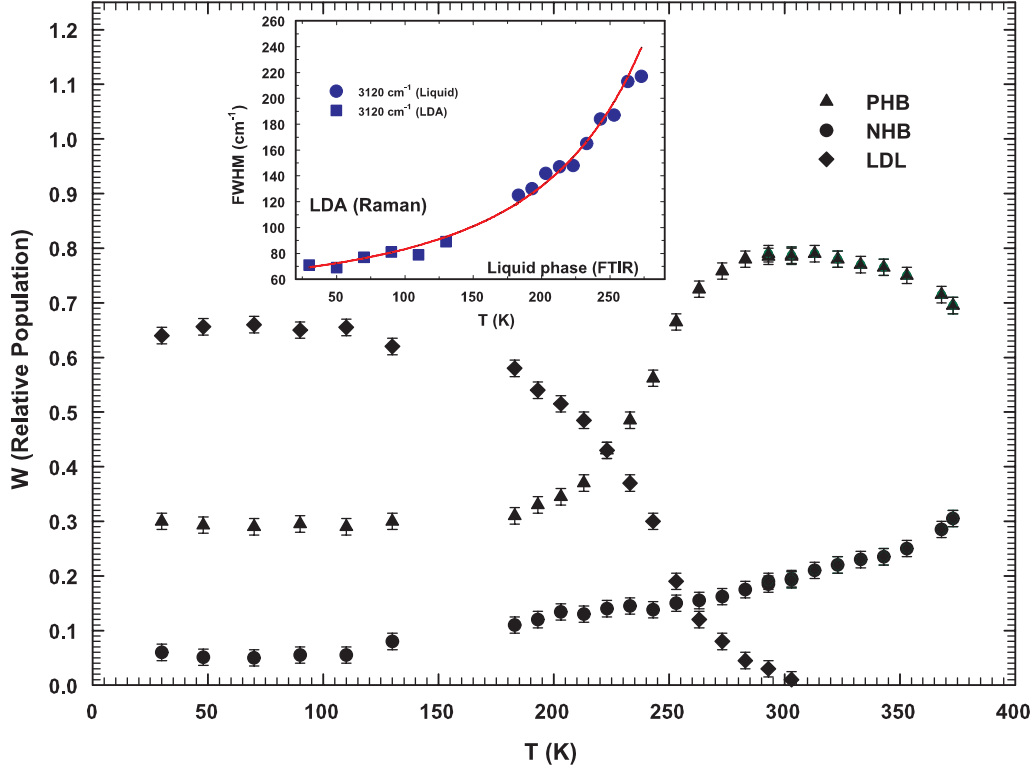
Fig. 7. Temperature dependence of the fractioned relative populations, W_{LDL}, of the LDL (diamonds) and W_{HDL} of the HDL (triangles and circles) water phases. For the HDL phase, NHB (circles) and PHB (triangles) contributions are reported separately. Inset: The FWHM values of OH stretching spectral component I ($3120\,\mathrm{cm}^{-1}$) vs. T, measured in the confined water and in the LDA phase [26,47].

measured in the LDA phase [47] and the one measured in MCM confined water [26]. The inset of Fig. 7 reports such a quantity vs. T in the interval $30\,\mathrm{K} < T < 290\,\mathrm{K}$. As it can be observed, the reported data can be certainly connected with continuity, from the liquid to the LDA region, by means of a unique analytical curve. The behaviour shown, indicates a direct link between the contribution (I) of the OHS spectrum and the LDL water phase, demonstrating the idea proposed by the LLPT hypothesis of a striking correspondence between LDA and LDL.

Next considerations are based on the fundamental law of the scattering theory for which the integrated intensity of the measured spectra $I(Q,\omega)$ is directly proportional to the number of the different species of scatterers. Namely, $I(Q,\omega) = (N/V)P(Q)S(Q,\omega)$, where $P(Q)$ is the scatterer form factor, while N denotes the number of scatterers in the scattering volume V. In Fig. 7 we report, in the interval $30\,\mathrm{K} < T < 373\,\mathrm{K}$, the fractional relative populations, W_{LDL}, of the LDL (diamonds) and W_{HDL} of the HDL (triangles and circles) water phases, calculated as the ratio of the component integrated area to the total OHS area. For the latter phase, NHB (circles) and PHB (triangles) contributions are reported separately. According to the scattering theory, the relative populations are defined as $W_i = N_i/N$, where N_i and N are the number of the particles of the phase i and the total number of scattering particles, respectively. Data are collected from different experiments: for the temperature region $30\,\mathrm{K}$–$130\,\mathrm{K}$ we used the data coming out from the analysis of OHS Raman of LDA spectra [47], for $183\,\mathrm{K} < T < 303\,\mathrm{K}$ we used our FTIR data on supercooled confined water [26], whereas for $253\,\mathrm{K} < T < 373\,\mathrm{K}$ we analysed Raman data of bulk water [43,44,46]. It is apparent that the thermal behaviour of all three species is continuous across the different temperature ranges, although coming from different data sets. This is of relevant interest, especially for the component (I), because it confirms the observation, in terms of the corresponding FWHM, that it is the LDL liquid phase. As it can be observed, the NHB and PHB contributions are present at all temperatures,

whereas the LDL phase exists only in the range 30K–303 K. The LDA phase is dominated by the LDL species, whereas in the stable liquid phase for $T > 303$ K only the HDL is present. The PHB population has a maximum at about 303 K, decreases on decreasing T in the entire supercooled region, crosses LDL at about 225 K, and finally becomes stable ($W \sim 0.29$) in the LDA phase.

From these results, it is evident that the HB random tetrahedral network is formed essentially inside the metastable supercooled regime. It is also important to note that NHB and PHB are also present in the LDA phase, indicating that the dynamics of LDA is not completely frozen even at $T = 30$ K, in agreement with experimental observations [58].

The results reported in the Fig. 7, can be used to obtain the H_2O density and to explore, by using optical methods, the possibility of a minimum in this thermodynamical variable. Very recently, the existence of a density minimum in the supercooled phase has been observed in confined D_2O by using neutron scattering at the temperature $T_{min} = (210 \pm 5)$ K [31]. The idea of a minimum, located approximately 70 K below the temperature of the density maximum T_{md}, has been also suggested by MD simulation studies [32], in which both the TIP5P-E and the ST2 potential models for water have been used [32,59]. Such a possibility may also be inferred from simple arguments on considering the density data of supercooled bulk water, ice Ih and LDA water [60]. After the maximum, the density of bulk water decreases rapidly with decreasing T before T_H, whereas the ice Ih has a smaller density than that of the liquid and, contrary to supercooled bulk water, has a normal positive expansivity, i.e. density increases as T decreases. The same behaviour is observed for LDA at its highest temperatures. From the structural point of view, Ice Ih represents the limiting case of a perfectly ordered tetrahedral network of HB, whereas LDA, that forms from deeply supercooled water, has a structure that very closely approaches that of a "random tetrahedral network" (RTN). Thus, ice Ih sets a lower bound for the density that the supercooled water could in principle attain. From these arguments, if the structure of deeply supercooled water approaches that of a RTN, and if nucleation can be avoided, it is then possible that a density minimum could occur in the deeply supercooled liquid.

Since only water contributes to the reported OHS spectra, its total density can be obtained only from the respective densities of its phases: the LDL and HDL. MD simulations [2], and proper neutron scattering data give estimated values of the corresponding densities [12]: $\rho_{HDL} \approx 1.2$ g/cm^3 and $\rho_{LDL} \approx 0.88$ g/cm^3. The density of LDA was experimentally measured as [61]: $\rho_{LDA} \approx 0.94$ g/cm^3. Since the LDL phase exists only for $T < 303$ K, the HDL water is only given for $T > 303$ K by the remaining spectral contributions classified as NHB and PHB.

Water density can be calculated from the fractionated populations W_{LDL} and W_{HDL} and their individual local densities ρ_{LDL} and ρ_{HDL}. The W quantities are T dependent in all the studied liquid regime and also the individual densities may in principle change with temperature. This may be verified on considering for instance the region $T > 303$ K, where only the PHB and NHB species contribute to the OHS spectra [43,44]. Thus, in the interval 303 K $< T < 373$ K, the densities ρ_{PHB} and ρ_{PNB} can be obtained from the bulk water density as: $\rho_{H_2O} = \rho_{PHB}W_{PHB} + \rho_{NHB}W_{NHB}$, being the $\rho_{H_2O}(T)$ values well known in the range 239 K $< T < 423$ K [62–64]. By considering all the W_{PHB} and W_{NHB} data points measured in that T interval, we obtain: $\rho_{PHB} \simeq 1.10 \pm 0.02$ g/cm^3 and $\rho_{NHB} \simeq 0.59 \pm 0.02$ g/cm^3. As a result, these values are temperature independent within the reported experimental error. This finding is not surprising, considering the literature data on proton magnetic resonance chemical shift of liquid water in a temperature range 273 K–363 K. This quantity, that as well known, entirely reflects the system local structure, does not exhibit any singularity or discontinuity in the above temperature range [65]. From this analysis we have that: (a) in the considered T range, ρ depends on T only through W; (b) $\rho_{NHB} \simeq 0.59 \pm 0.02$ g/cm^3, according to Kell's representation [62] of bulk water density as a function of T, corresponds to the density value of H_2O at $T \sim 625$ K. Such a value is smaller than that used (0.66 g/cm^3 for $T = 673$ K, at a pressure of 800 bar) in a neutron scattering experiment in the supercritical region, where no distinct HB peaks are observable in the O-H radial distribution function g_{OH} [66]. Thus, the value of ρ_{NHB} reasonably represents that of NHB water, which dominates vibrational spectra in the region above the critical temperature (C). In addition, $\rho_{PHB} \simeq 1.10 \pm 0.02$ g/cm^3 is
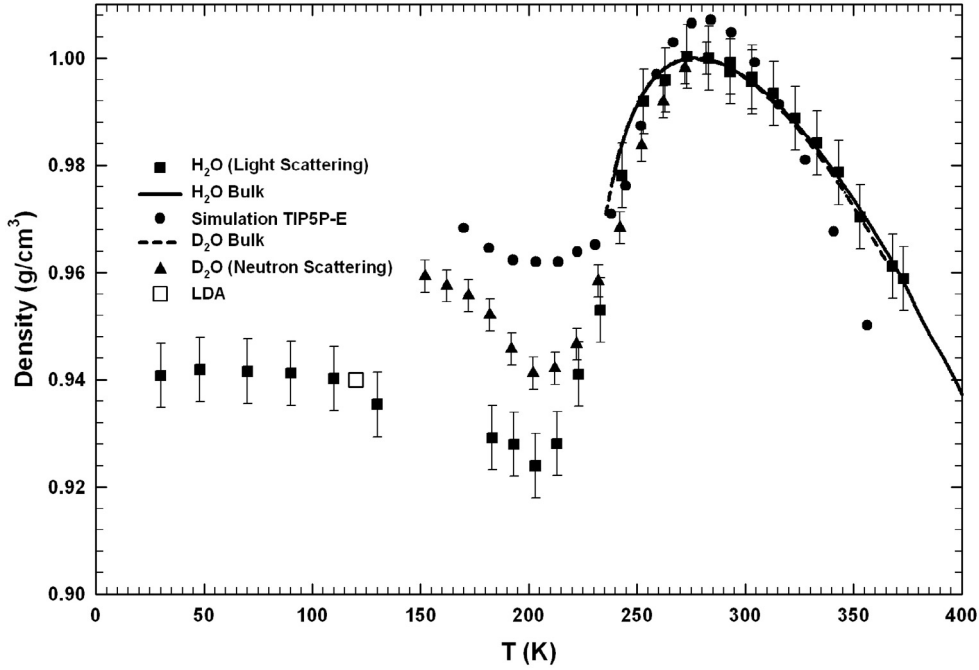
Fig. 8. The measured $\rho_{H_2O}(T)$ vs. T (squares). The solid and dotted lines refer to bulk densities of H_2O and D_2O, respectively [62–64]. Triangles represent the $\rho_{D_2O}(T)$ measured by means of neutron scattering [18]. The dots mark the bulk density values calculated by the MD simulation [32]. The open square represents the density of the LDA water at $T = 120\,K$ [61]. Heavy water densities are properly scaled with respect to ρ_{H_2O}.

comparable with the value proposed for the HDL water [12]. Therefore, the contribution of HDL to the total H_2O density, Δ_{HDL}, can be obtained in all the explored T range ($30\,K < T < 373\,K$), by extending the calculation made for ρ_{NHB} and ρ_{PHB} to the lowest temperatures. By using similar arguments the density value of the ρ_{LDL} contribution of that phase, Δ_{LDL}, to the total ρ_{H_2O} has been calculated. In that case, we have considered the H_2O density values at temperatures around T_{md} [62], obtaining $\rho_{LDL} = 0.87 \pm 0.02\,g/cm^3$ [68], a value that closely matches that proposed by neutron diffraction data analysis for LDL water [12]. Thus ρ_{H_2O} has been calculated as $\rho_{H_2O} = \Delta_{HDL} + \Delta_{LDL}$ for the temperature interval $30\,K < T < 370\,K$.

Figure 8 reports the plot of the obtained water density vs. T. For comparison, we also report the values measured in bulk water in the range $239\,K < T < 423\,K$ [62,63]. As it can be observed, there is a good agreement between these "optically-measured" density data and the literature ones for ρ_{H_2O} in the supercooled regime (where, contrary to the range 273–373 K, data were not used to extract the values of ρ_{NHB}, ρ_{PHB} and ρ_{LDL}). Two findings are remarkable: the minimum at about $203 \pm 5\,K$ and the value of $\rho = 0.940 \pm 0.003\,g/cm^3$ in the LDA phase, nearly the same as that measured in the LDA ice at $T = 120\,K$ [61]. This result, together with those obtained for $T > 303\,K$, confirms that the LDL and HDL local structures are essentially temperature independent so that the thermal evolution of water density comes only from that of W_{LDL} and W_{HDL}. Looking carefully at the data in the region of deep supercooling (around 250 K) it is possible to observe that our data, evaluated for confined water, are slightly lower than those measured in bulk; this may be due to the confinement effect of water inside the nanotubes. However, the difference is not relevant enough to affect the overall result. In the same figure the $\rho_{D_2O}(T)$ data obtained by neutron measurements [18] and the results of the quoted MD simulation of H_2O with the TIP5P-E potential are also reported [32]. The ρ_{D_2O} data have been properly scaled over the ρ_{H_2O} taking into account the temperature shift of the corresponding maxima (about 7 K) and the absolute value of the $\rho_{D_2O}^{Maximum}$. As it can be observed there is a good agreement in the overall thermal behaviour between the $\rho_{D_2O}(T)$ and

$\rho_{\mathrm{H_2O}}(T)$ data, with the only difference that $\rho_{\mathrm{H_2O}}(T)$ includes the densities within the LDA phase. There is a marked difference between the experimental densities and MD simulation ones [32]. It is reasonably possible that, with the use of another water potential, MD simulation might give more reliable results compared with the experimental ones.

5 Concluding remarks

By exploring the dynamical properties of water in the deeply supercooled regime by means of separated NMR and QENS experiments, we give a conclusive proof of the existence of a FSC. The coincidence of this singularity with the BSE at the same T_{WL}, supports the LLPT theory according to which liquid water consists of a mixture of two different local liquid structures (the LDL and HDL phases). A remarkable result is the presence of the dynamical heterogeneities accompanying the BSE, that can be reasonably related with the onset of the LDL water phase dominating the local molecular structure below T_M. This result certainly constitutes a new element which can further clarify one of the intriguing properties of water.

References

1. C.A. Angell, in *Water: A Comprehensive Treatise*, Vol. 7, edited by F. Franks (Plenum, New York, 1982), pp. 1–81
2. P.G. Debenedetti, H.E. Stanley, Phys. Today **56**, 40 (2003)
3. O. Mishima, H.E. Stanley, Nature **396**, 329 (1998)
4. R.J. Speedy, J. Phys. Chem. **86**, 982 (1982)
5. H.E. Stanley, J. Teixeira, J. Chem. Phys. **73** (1980)
6. P.H. Poole, F. Sciortino, U. Essmann, H.E. Stanley, Nature **360**, 324 (1992)
7. C.T. Moynihan, Mater. Res. Soc. Symp. Proc. **455**, 411 (1997)
8. P.H. Poole, F. Sciortino, T. Grande, H.E. Stanley, C.A. Angell, Phys. Rev. Lett. **73**, 1632 (1994)
9. S.S. Borick, P.G. Debenedetti, S.A. Sastry, J. Phys. Chem. **99**, 3781 (1995)
10. O. Mishima, J. Chem. Phys. **100**, 5910 (1994)
11. O. Mishima, H.E. Stanley, Nature **392**, 164 (1998)
12. A.K. Soper, M.A. Ricci, Phys. Rev. Lett. **84**, 2881 (2000)
13. E. Trinh, R.E. Apfel, J. Chem. Phys. **72**, 6731 (1980)
14. M. Yamada, S. Massa, H.E. Stanley, F. Sciortino, Phys. Rev. Lett. **88**, 195701 (2002)
15. R. Bergman, J. Swenson, Nature **403**, 283 (2000)
16. K. Koga, H. Tanaka, X.C. Zeng, Nature **408**, 564 (2000)
17. B. Webber, J. Dore, J. Phys.: Cond. Matter **16**, S5449 (2004)
18. L. Liu, S.H. Chen, A. Faraone, C.W. Yen, C.-Y. Mou, Phys. Rev. Lett. **95**, 117802 (2005)
19. F. Mallamace, M. Broccio, C. Corsaro, A. Faraone, U. Wanderlingh, L. Liu, C.-Y. Mou, S.-H. Chen, J. Chem. Phys. **124**, 161102 (2006)
20. L.M. Xu, P. Kumar, S.V. Buldyrev, S.H. Chen, P.H. Poole, F. Sciortino, H.E. Stanley, PNAS **102**, 16558 (2005)
21. C.A. Angell, Ann. Rev. Phys. Chem. **55**, 559 (2004)
22. P.G. Debenedetti, J. Phys.: Cond. Matter **15**, R1669 (2003)
23. P. Kumar, S.V. Buldyrev, F. Starr, N. Giovanbattista, H.E. Stanley, Phys. Rev. E **72**, 051503 (2005)
24. K. Ito, C.T. Moynihan, C.A. Angell, Nature **398**, 492 (1999)
25. S.-H. Chen, F. Mallamace, C.-Y. Mou, M. Broccio, C. Corsaro, A. Faraone, L. Liu, PNAS **103**, 12974 (2006)
26. F. Mallamace, M. Broccio, C. Corsaro, A. Faraone, D. Majolino, V. Venuti, L. Liu, C.-Y. Mou, S.-H. Chen, PNAS **104**, 428 (2007)

27. S.H. Chen, L. Liu, E. Fratini, P. Baglioni, A. Faraone, E. Mamantov, PNAS **103**, 9012 (2006)
28. P. Kumar, Z. Yan, L. Xu, M.G. Mazza, S.V. Buldyrev, S.H. Chen, S. Sastry, H.E. Stanley, Phys. Rev. Lett. **97**, 177802 (2006)
29. G. Franzese, H.E. Stanley, J. Phys.: Cond. Matter **19**, 205126 (2007)
30. P. Kumar, Z. Yan, L. Xu, M.G. Mazza, S.V. Buldyrev, S.H. Chen, S. Sastry, H.E. Stanley, in *Soft Matter under Extreme Pressure: Fundamental and Emerging Technologies*, edited by S.J. Rzoska, V. Mazur (Springer, Berlin, 2005)
31. L. Liu, Y. Zhang, C.C. Chen, C.-Y. Mou, P.H. Poole, C.-H. Chen, PNAS **104**, 9570 (2007)
32. D. Paschek, Phys. Rev. Lett. **94**, 217802 (2005)
33. D.A. Fuentevilla, M.A. Anisimov, Phys. Rev. Lett. **97**, 195702 (2006)
34. K. Morishige, K. Nobuoca, J. Chem. Phys. **107**, 6965 (1997)
35. A. Schreiber, I. Ketelsen, G.H. Findenegg, Phys. Chem. Chem. Phys. **3**, 1185 (2001)
36. K. Overloop, L. van Gerven, J. Mag. Res. A **101**, 147 (1993)
37. E.W. Hansen, R. Schmidt, M. Stöcker, D. Akporiaye, J. Phys. Chem. **99**, 4148 (1995)
38. J.M. Zanotti, M.C. Bellissent-Funel, S.H. Chen, Europhys. Lett. **71**, 91 (2005)
39. B. Grünberg, T. Emmler, E. Gedat, J. Shenderovich, G.H. Findenegg, H.H. Limbach, G. Buntkowsky, Chem. Eur. J **10**, 5689 (2004)
40. L. Liu, A. Faraone, S.H. Chen, Phys. Rev. E **65**, 041506 (2002)
41. M.C. Bellissent-Funel, S.H. Chen, J.M. Zanotti, Phys. Rev. E **51**, 4558 (1995)
42. L. Bosio, S.H. Chen, J. Teixeira, Phys. Rev. A **27**, 1468 (1983)
43. G.E. Walrafen, J. Chem. Phys. **47**, 114 (1967); G.E. Walrafen, M.R. Fisher, M.S. Hokmabadi, B.-H. Yang, J. Chem. Phys. **85**, 6970 (1986)
44. G. D' Arrigo, G. Maisano, F. Mallamace, P. Migliardo, F. Wanderlingh, J. Chem. Phys. **75**, 4264 (1985)
45. J.B. Brubach, A. Mermet, A. Filabozzi, A. Gerschel, P. Roy, J. Chem. Phys. **122**, 184509 (2005)
46. G.E. Walrafen, in *Structure of Water and Aqueous Solutions*, edited by W.A.P. Luck (Verlag Chemie, Weinheim, 1974)
47. C.G. Venkatesh, S.A. Rice, J.B. Bates, J. Chem. Phys. **63**, 1065 (1975); T.C. Sivakumar, S.A. Rice, M.G. Sceats, J. Chem. Phys. **69**, 3468 (1978)
48. M.D. Ediger, Ann. Rev. Phys. Chem. **51**, 99 (2000)
49. F. Fujara, B. Geil, H. Sillescu, G. Fleishcer, Z. Phys. B **88**, 195 (1992)
50. S.F. Swallen, P.A. Bonvallet, R.J. McMahon, M.D. Ediger, Phys. Rev. Lett. **90**, 01590 (2003)
51. J. Chang, H. Sillescu, J. Phys. Chem. B **101**, 8794 (1997)
52. M.T. Cicerone, M.D. Ediger, J. Chem. Phys. **104**, 7210 (1996)
53. X.Y. Xia, P.G. Wolynes, J. Phys. Chem. B **105**, 6570 (2001)
54. K.L. Ngai, J.H. Magill, D.J. Plazek, J. Chem. Phys. **112**, 1887 (2000)
55. A.C. Pan, J.P. Garrahan, D. Chandler, Chem. Phys. Chem. **6**, 1783 (2005)
56. Y.-J. Jung, J.P. Garrahan, D. Chandler, Phys. Rev. E **69**, 061205 (2004)
57. R. Yamamoto, A. Onuki, Phys. Rev. Lett. **81**, 4915 (1998)
58. R.S. Smith, C. Huang, B.D. Kay, J. Phys. Chem. B **101**, 6123 (1997)
59. P.H. Poole, I. Saika-Voivoid, F. Sciortino, J. Phys. Cond. Matter **17**, L431 (2005)
60. C.A. Angell, R.D. Bressel, M. Hemmati, E.J. Sare, J.C. Tucker, Phys. Chem. Chem. Phys. **2**, 1559 (2000)
61. M.A. Floriano, Y.P. Handa, D.D. Klug, E. Whalley, J. Chem. Phys. **91**, 7187 (1989)
62. G.S. Kell, J. Chem. Eng. Data **12**, 66 (1989); J. Chem. Eng. Data **20**, 97 (1975)
63. C.M. Sorensen, J. Chem. Phys. **79**, 1455 (1983)
64. M. Vedamuthu, S. Singh, G.W. Robinson, J. Phys. Chem. **100**, 3825 (1996)
65. K. Modig, B. Pfrommer, B. Halle, Phys. Rev. Lett. **90**, 075502 (2003)
66. A.K. Soper, F. Bruni, M.A. Ricci, J. Chem. Phys. **106**, 247 (1997)
67. P. Kumar, S. Buldyrev, S.R. Becker, P.H. Poole, F.W. Starr, H.E. Stanley, PNAS **104**, 9575 (2007)
68. F. Mallamace, C. Branca, M. Broccio, C. Corsaro, C.-Y. Mou, S.-H. Chen, PNAS **104**, 18387 (2007)